Novel regenerable sorbent based on Zr–Mn binary metal oxides for flue gas mercury retention and recovery

Jiangkun Xie, Zan Qu*, Naiqiang Yan*, Shijian Yang, Wanmiao Chen, Lingang Hu, Wenjun Huang, Ping Liu

School of Environmental Science and Engineering, Shanghai Jiao Tong University, Shanghai 200240, China

HIGHLIGHTS

- Zr–Mn binary oxides are found performing much better than manganese oxide.
- Higher BET area and more high-valence manganese play important role in mercury capture.
- O_2 could promote the oxidation of mercury while SO_2 would inhibit the mercury sorption.
- Spent sorbent could be facilely revivified by heating and washing treatment.

ARTICLE INFO

ABSTRACT

To capture and recover mercury from coal-fired flue gas, a series of novel regenerable sorbents based on Zr–Mn binary metal oxides were prepared and employed at a relatively low temperature. PXRD, TEM, TPR, XPS, and N_2-adsorption methods were employed to characterize the sorbents. The Hg^0 adsorption performance of the sorbents was tested, and the effects of the main operation parameters and the gas components on the adsorption were investigated. Zr significantly improved the sorbent's mercury capacity, which was nearly 5 mg/g for $Zr_{0.5}Mn_{0.5}O_y$. Furthermore, the spent sorbent could be regenerated by heating to 350 °C, and the highly concentrated elemental mercury released could be facilely recycled. Therefore, a much greener process for mercury capture and recovery could be anticipated based on this regenerable sorbent.

1. Introduction

The environmental hazard of mercury has attracted increasing concern since Minamata disease first emerged in Japan in the 1950s. Mercury has been classified as a high-priority pollutant in many countries [1–5], and an international treaty on mercury pollution will soon be agreed upon. The US EPA issued the first national standards for mercury pollution from power plants in 2011. As the largest mercury emission country in the world, China's government has also paid increasing attention to mercury control. In particular, the newly issued "Emission Standard of Air Pollutants for Thermal Power Plants" (GB13223-2011) capped mercury emissions. According to statistics, the main anthropogenic emitters of mercury in China are coal-fired power plants and sintering processes, among which most mercury was discharged with flue gases [6]. The emission reduction of these sources is of great significance for the control of mercury emissions in China.

The existing forms of mercury in various flue gases are elemental mercury (Hg^0), oxidized mercury (Hg^{2+}), and particulate-bound mercury (Hg^p) [7]. Most of the oxidized mercury is soluble in water and can be removed through wet scrubber processes, and particulate-bound mercury can be captured by ESP (electrostatic precipitation) or bag house devices. Thus, elemental mercury, which is neither soluble in water nor removable by ESP, is the most intractable issue for mercury removal.

The state-of-art technology for flue gas mercury capture mainly focuses on two groups: the co-benefit of SCR (selective catalytic reduction), ESP and FGD (flue gas desulfurization), and activated carbon injection (ACI). The combination of SCR, ESP, and FGD first oxidizes the elemental mercury in the flue gas over an SCR catalyst and then captures the oxidized mercury through ESP or FGD. However, suitable catalysts are still under development, and this process only transfers gaseous mercury into fly ash, desulfurization slurry, or gypsum and therefore may cause secondary pollution [8,9]. ACI produces high-efficiency mercury removal from flue gas, but the economic value of fly ash is sacrificed due to its mixing with contaminated activated carbon powder.

* Corresponding authors. Tel.: +86 021 54745591; fax: +86 021 54745591.
E-mail addresses: quzan@sjtu.edu.cn (Z. Qu), nqyan@sjtu.edu.cn (N. Yan).

Therefore, the development of a new process for flue gas mercury removal is of great significance. A sorption and desorption cycle based on a regenerable sorbent may be a more ideal mercury control process due to its facile operation and low cost. Sorbents are the core of sorption and desorption processes for mercury removal from flue gas. Previous studies have reported on silver- or gold-based sorbents that could be regenerated through heating [10–14]. However, the mercury capacity of the sorbents still needs improvement for industrial application, and the cost of noble metals also limits their practical application. Therefore, developing regenerable sorbents with high mercury capacity is the key for the industrialization of sorption and desorption processes [10,12,13,15]. ZrO_2 nanoparticles are also an important topic because of their applicability in high surface area catalysts, optical and electronic nano devices [16,17]. In our previous work [18,19], manganese oxide modified with different metals showed varying mercury removal capacities. The doping of zirconium into manganese oxide is interesting as a possible way to improve the sorbent's performance; however, the performance of Zr–Mn binary metal oxides for mercury capture has not yet been studied.

Herein, a series of novel sorbents were prepared, and their mercury capacities were investigated to assess their potential for mercury capture applications. The impact of space velocity on the removal efficiency and the influence of flue gas components, including SO_2 and O_2, on the mercury capacity were experimentally studied. The regenerability of the sorbent and the optimum temperature for sorbent regeneration were also investigated.

2. Experimental

2.1. Sorbent preparation

The sorbents were prepared through the co-precipitation method. The process is briefly described as follows. A given amount of mixed metal nitrates was added to deionized water under stirring until it was completely dissolved, after which the stoichiometric amount of ammonia was added to the solution as the precipitation agent under strong stirring for 2 h. For $Zr_{0.5}Mn_{0.5}O_y$, 20 mmol of $Zr(NO_3)_4$ and 20 mmol of $Mn(NO_3)_2$ were dissolved in 80 ml of deionized water under stirring, after which 120 mmol of ammonia was added to the mixed solution under strong stirring for 2 h. The precipitate was filtrated and washed 3 times with deionized water, and the precipitate was transferred to a muffle furnace and calcined at 500 °C for 5 h. ZrO_2, $Zr_{0.25}Mn_{0.75}O_y$, $Zr_{0.75}Mn_{0.25}O_y$, and MnO_x were prepared using the same procedure except with different amounts of mixed metal nitrates and ammonia. All the samples were ground to 40–60 mesh.

2.2. Sorbent characterization

Powder X-ray diffraction patterns (PXRD) were obtained on a Rigaku D/max-2200/PC powder diffractometer using Cu Kα radiation (40 kV and 20 mA). A glass holder was used to support the samples. The scanning range was from 10° to 80° with a scanning velocity of 7° min^{-1}. The XRD phases present in the samples were identified with the help of JCPDS data files. The microstructure of the sorbents was characterized by transmission electron microscopy (TEM). Samples were dispersed in ethanol with strong sonication before the analysis, and the data were collected on a JEM-2100 instrument (Japan, 20 kV). Nitrogen adsorption and desorption isotherms were recorded using a nitrogen adsorption apparatus (Quantachrome Nova 2200e) at −196 °C (the temperature of the liquid nitrogen bath). All samples were degassed for 3 h at 200 °C before testing. The specific surface areas of the sorbents were calculated using the Brunauer–Emmett–Teller (BET)

method, and the pore volume and average pore size were calculated using the Barrett–Joyner–Halenda (BJH) model. X-ray photoelectron spectroscopy (XPS) measurements were made using an AXIS Ultra^{DLD} (Shimadzu–Kratos) spectrometer with Al Kα as the excitation source. The C 1s line at 284.6 eV was used as a reference for the binding energy calibration. TPR (temperature programmed reduction) tests were performed on a Micromeritics ChemiSorp 2720 TPx instrument with 10% H_2/N_2 gaseous mixture as the reductant. The ramp rate was 10 °C/min from 50 to 900 °C. Samples were purged with N_2 flow at 300 °C for 2 h before testing. Differential pulse voltammetry (DPV) curves were obtained using a CHI-650D electrochemical workstation (Shanghai Chenhua) in KCl solution with glass carbon as the working electrode, platinum wire as the auxiliary electrode, and Ag/AgCl as the reference electrode. The amplitude was 0.05 V, and the pulse width was 0.05 s.

2.3. Mercury capacity evaluation

The assembly used for elemental mercury capture consisted of an elemental mercury permeation tube, a packed-bed reactor with a parallel blank tube, a cold vapor atomic absorption spectrometer (CVAAS), and an online data acquisition system. A tubular furnace was employed to maintain the reactor at the desired temperature. N_2 was used as the carrier gas to yield a stable concentration of elemental mercury. First, the signal baseline was calibrated by bypassing the carrier gas from the mercury permeation tube, and the carrier gas was then diverted into the mercury permeation tube to generate a stable mercury concentration. Next, gaseous influent with a stable mercury concentration was diverted into the packed-bed reactor and the breakthrough curves were recorded by an online data acquisition system. The reactor was packed with a given amount of sorbents, and silicon wool was used as the support to prevent sorbent loss. To create a mercury balance, a reducing bottle containing $SnCl_2$ solution was placed after the outlet of the first CVAAS detector, and another CVAAS detector was used in tandem with the first one. The signal from the second detector was almost the same as that from the first detector; therefore, the Hg^{2+} escaping from the sorbent-filled bed in this experiment was considered to be negligible, and the influent mercury was approximated as equal to the adsorbed mercury plus the escaped Hg^0. To investigate the effect of flue gas components, the breakthrough curves of elemental mercury on $Zr_{1−x}Mn_xO_y$ during the test time (10 h) were integrated and compared, and the adsorption capacities of the mercury were calculated according to Eq. (1). The adsorption capacity was defined as the mass of elemental mercury that was converted into HgO or other forms per mass of sorbent and was calculated as follows:

$$Q = \frac{1}{m} \int_{t_0}^{t_1} (Hg^0_{inlet} - Hg^0_{outlet}) \times f \times dt \tag{1}$$

where Q is the adsorption capacity, m is mass of the catalysts (20 mg in this experiment), f denotes the flow rate of the influent, and t_0 and t_1 represent the initial and final times of the breakthrough curves, respectively. The inlet Hg^0 concentration was approximately 0.9 ± 0.05 mg/m^3 (calibrated by Lumex RA 915$^+$). It was found that the capacity calculated here was consistent with the results calculated from Lumex-Pyro-915$^+$ (relative deviation < 5%).

The process flow of packed bed experiments is sketched in Fig. 1.

3. Results and discussion

3.1. Characterization results

PXRD patterns were used to characterize the structure of the sorbents, as shown in Fig. S1. Zirconium oxide existed in the form of
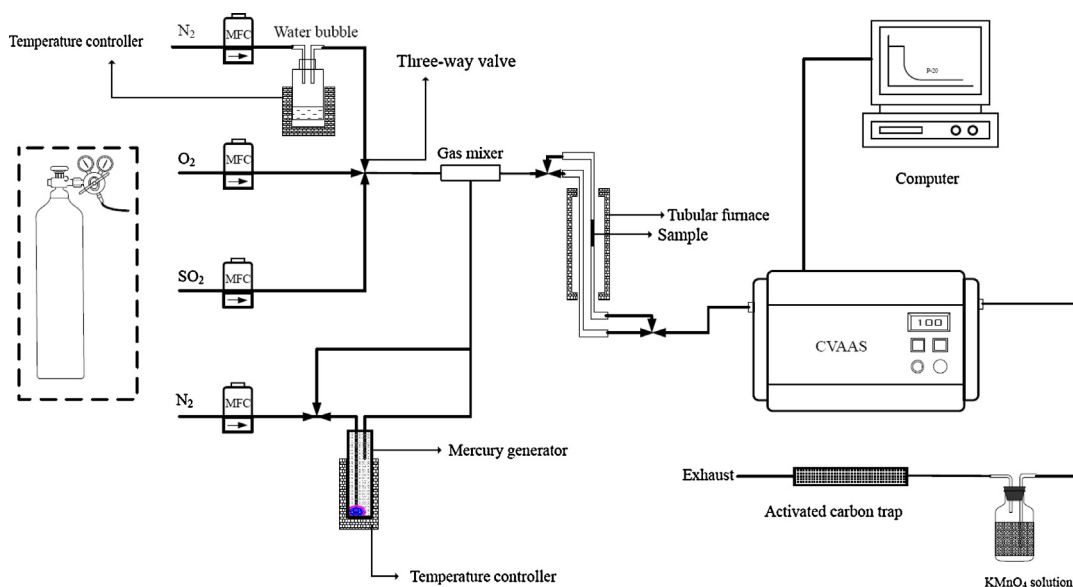
Fig. 1. Process flow of the mercury capacity assessment system.

ZrO_2, which conforms to pdf no. 651023, whereas manganese oxide consisted of a mixture of Mn_2O_3 (pdf no. 240508) and Mn_3O_4 (pdf no. 160154). After doping zirconium into the manganese oxides, the amorphous phase overwhelmed the sorbent, and almost no peak attributed to the crystal phase was observed. The doped zirconium may have interacted with manganese oxide and prevented manganese oxide from crystallizing, resulting in small amorphous binary oxides. Although the prevalence of the amorphous phase made it more difficult to identify the structure of the sorbents, smaller amorphous particles may benefit the sorption performance due to its high surface area.

The sorbent particle size may play an important role in the adsorption capacity of the sorbent. Therefore, the microstructural morphology of the sorbents was further characterized by TEM. As illustrated in Fig. 2, although all of the sorbents used in this study were nano-scaled, they still differed greatly in size. The single metal oxide (MnO_x) particles were much larger than the mixed metal oxide particles. It was speculated that the doping of zirconium into manganese oxide and the interaction between zirconium and manganese prevented the crystallization of the binary oxides and particle aggregation. As a consequence, the amorphous phase was favored and smaller particles tended to form.

Surface area is another key parameter for a sorbent; larger surface areas provide many more active sites for interactions between the sorbent and sorbate, which usually leads to better sorption or catalytic performance. As shown in Table 1, the specific surface areas of the single metal oxides (ZrO_2 and MnO_x) were much smaller than those of the mixed metal oxides. This finding was consistent with the TEM results, which showed that smaller particles had higher specific surface areas. In general, the surface areas of the mixed metal oxides were much higher than those of the single metal oxides. For example, the surface area

of $Zr_{0.5}Mn_{0.5}O_y$ (approximately 150 m^2/g) was much higher than that of MnO_x (approximately 5 m^2/g). Although the surface area was not the only factor that affected the sorbent capacity, it was one of the most important.

To characterize the reducibility of the sorbent, H_2-TPR curves were recorded from 50 to 900 °C. As shown in Fig. 3, the two reducing peaks of MnO_x at approximately 370 and 520 °C could attributed to Mn^{4+} reducing to Mn^{3+} and Mn^{3+} reducing to Mn^{2+}, respectively [20,21]. Only one reducing peak was observed for the ZrO_2 sample, which was located above 600 °C. These results indicated that MnO_x was chemically active whereas pure ZrO_2 was relatively inert. However, it was interesting that the doping of inert zirconium into manganese oxide modified the reducibility of the binary metal oxides. The reducing peaks of $Zr_{0.25}Mn_{0.75}O_y$ and $Zr_{0.5}Mn_{0.5}O_y$ shifted substantially toward lower temperatures. Although this shift for $Zr_{0.75}Mn_{0.25}O_y$ was less obvious, the shape of the reducing peak was modified relative to that of MnO_x. The result supported the existence of an interaction between zirconium and manganese in the binary metal oxides. Furthermore, the ratio of Mn^{4+}/Mn^{3+} was calculated by integrating the areas of the reducing peaks, and the results were listed in Table 2. The results revealed that the doping of zirconium could significantly increase the Mn^{4+} content relative to low-oxidation-state manganese species in the binary metal oxides. In summary, the doping of zirconium could not only enhance the reducibility but also facilitate the formation of high-oxidation-state manganese.

The XPS spectra were obtained for the O 1s, S 2p, Hg 4f, and Mn 2p regions to characterize the valence change before and after adsorption. As shown in Fig. 4, for the fresh $Zr_{0.5}Mn_{0.5}O_y$, the peaks at 229.8 and 531.1 eV for O 1s could be attributed to transition metal oxides and –OH, respectively [11,19,22]. After adsorbing mercury in the presence of 500 ppm SO_2, an emerging peak was observed at 532.3 eV, which was attributed to oxygen in SO_4^{2-}. This finding

Table 1
N_2 adsorption and desorption results of $Zr_{1-x}Mn_xO_y$.

	BET surface area (m^2/g)	Average pore size (nm)	Pore volume (ml/g)
ZrO_2	28.460	11.440	0.208
$Zr_{0.75}Mn_{0.25}O_y$	144.499	4.726	0.261
$Zr_{0.5}Mn_{0.5}O_y$	148.912	4.804	0.291
$Zr_{0.25}Mn_{0.75}O_y$	127.403	6.335	0.355
MnO_x	5.338	3.719	0.080

Table 2
Mn^{4+}/Mn^{3+} ratio calculated by the integration of TPR peak areas.

Sample	Mn^{4+}/Mn^{3+}
$Zr_{0.75}Mn_{0.25}O_y$	>100
$Zr_{0.5}Mn_{0.5}O_y$	≈10:1
$Zr_{0.25}Mn_{0.75}O_y$	≈1.5:1
MnO_x	≈0.25:1

MnO$_x$

Zr$_{0.25}$Mn$_{0.75}$O$_y$

Zr$_{0.5}$Mn$_{0.5}$O$_y$
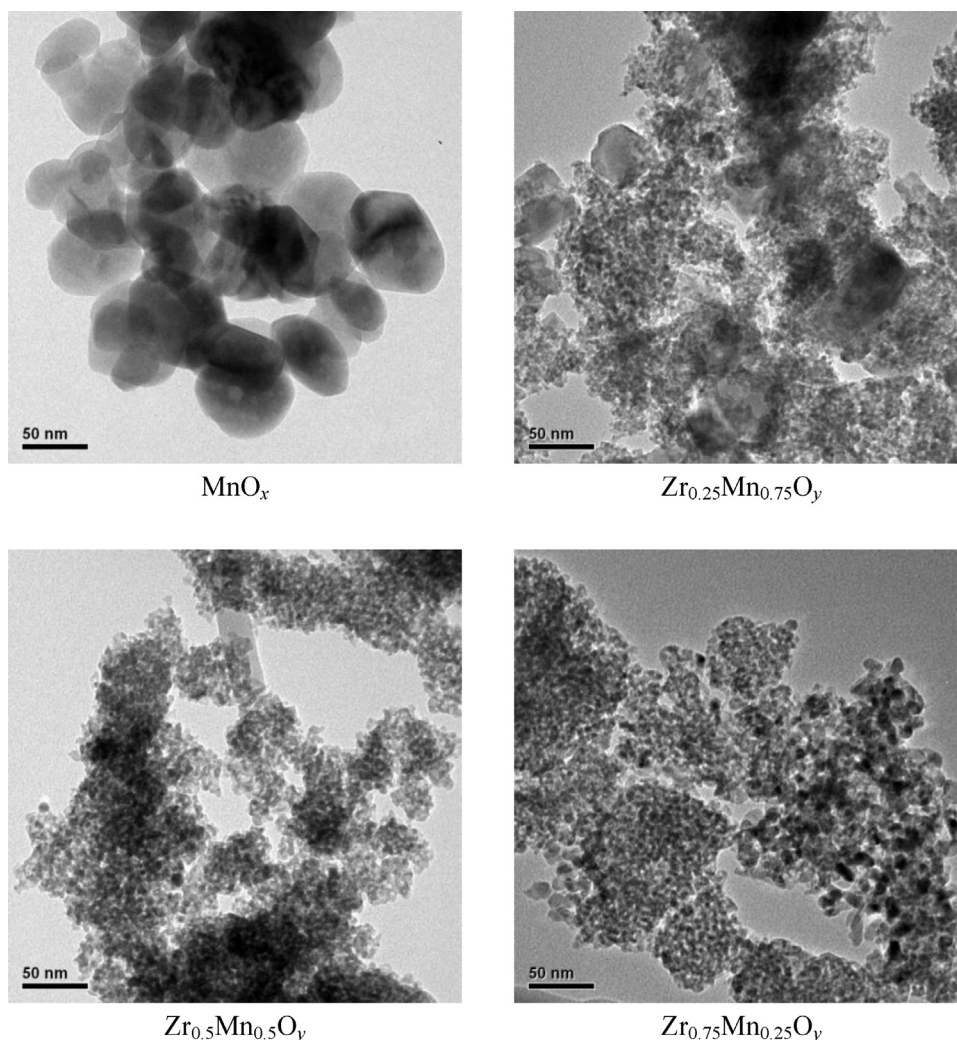

Zr$_{0.75}$Mn$_{0.25}$O$_y$

Fig. 2. TEM images of manganese-based sorbents.

illustrated that metal sulfate formed on the sorbent surface during the adsorption process in the presence of SO$_2$.

The formation of metal sulfate was also supported by the S 2p spectra. When the sorption was carried out without SO$_2$, no peak was observed in the S 2p binding energy region. When the reaction

Fig. 3. H$_2$-TPR curves of sorbents.

occurred in the presence of SO$_2$, peaks at 168.7 and 169.9 eV appeared, which could be attributed to the sulfur of SO$_4^{2-}$ and HSO$_4^{-}$, respectively [11,19,22].

Hg 4f spectra were also collected to analyze the mercury species on the sorbent surface. After mercury sorption, peaks at 101.3 and 105.5 eV were observed, which could be attributed to Hg 4f 7/2 and Hg 4f 5/2, respectively [11,19,22]. No other significant peak could be observed. This finding indicated that HgO was the main mercury species at the sorbent surface after mercury sorption. After desorption at 350 °C, no significant peak corresponding to HgO could be observed. This result demonstrated that the adsorbed mercury could be facilely released by proper heating.

The XPS spectra of Mn 2p also provided some interesting information (see Table 3 for detailed results). Manganese mainly existed as Mn^{4+} (642.2 eV) in fresh Zr$_{0.5}$Mn$_{0.5}$O$_y$. After adsorbing mercury
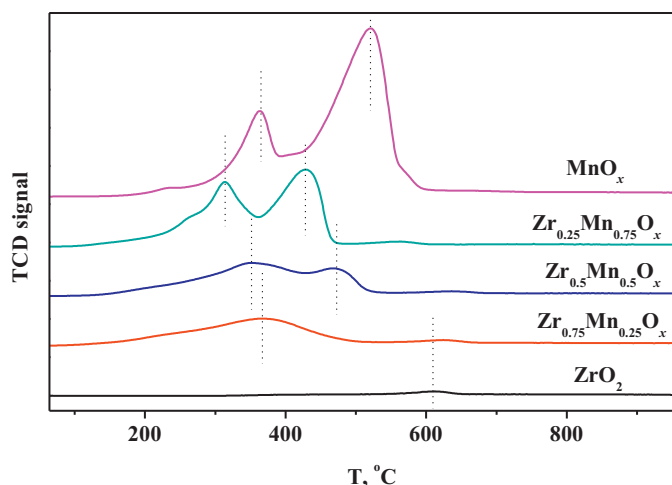
Table 3
Manganese species distribution calculated by XPS results.

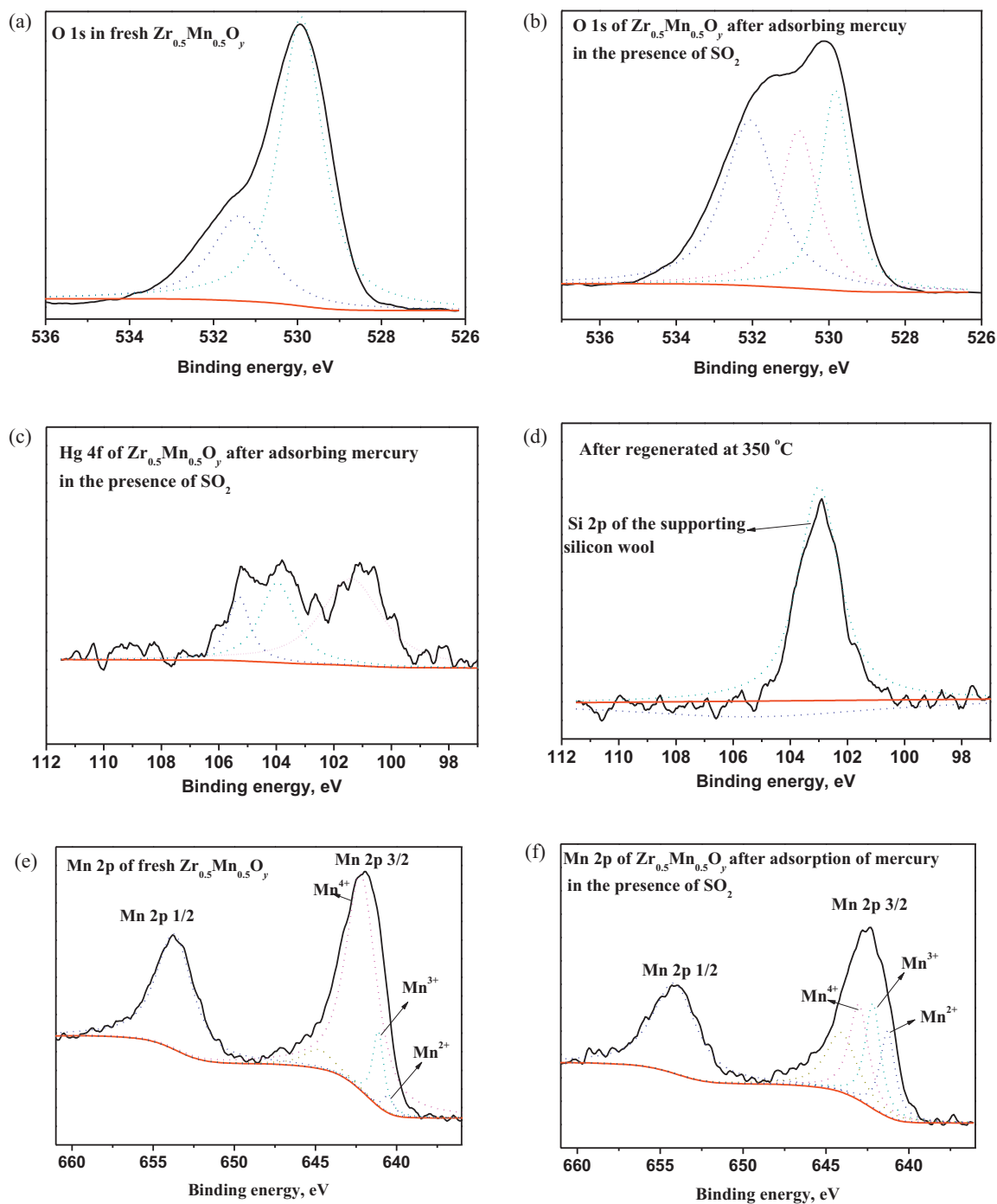| Sample	Mn^{4+}	Mn^{3+}	Mn^{2+}
Fresh Zr$_{0.5}$Mn$_{0.5}$O$_y$	87%	11%	2%
After adsorbing mercury in N$_2$	71%	22%	7%
After adsorbing mercury in N$_2$ + O$_2$	72%	4%	24%
After adsorbing mercury in N$_2$ + O$_2$ + SO$_2$	39%	34%	27%
After desorption at 350 °C	39%	32%	30%

Fig. 4. XPS spectra of O 1s, S 2p, Mn 2p, and Hg 4f.

at 100 °C for 10 h in the absence of O_2, the Mn^{4+} surface content decreased, mostly through reduction to Mn^{3+}. However, if the mercury sorption was carried out in the presence of 4% O_2, the Mn^{3+} formed could be further reduced to Mn^{2+}. It was speculated O_2 could catalyze the reaction that Mn^{3+} oxidize Hg^0 on the surface of $Zr_{0.5}Mn_{0.5}O_y$. For this reason, O_2 could improve the capability of the sorbent to oxidize mercury. This mechanism could explain why O_2 had a positive effect on the mercury capacity of the sorbent. Furthermore, if 4% O_2 and 500 ppm SO_2 were added into the influent gas, the mercury capacity of the sorbent decreased slightly. It was believed that SO_2 competitively occupied the active sites on sorbent surface, which would prevent mercury from reacting with the active manganese species.

Combining the XPS and TPR results with the macro-experimental data, the following could be proposed as the main pathway for mercury retention on the sorbent. Gaseous elemental mercury adsorbed on sorbent surface and was then oxidized to HgO by zirconium-modified MnO_2 with the assistance of O_2. Meanwhile, MnO_2 was reduced to MnO and thereby lost its mercury capture activity. SO_2 could compete with elemental mercury for active sites on sorbent surface and inhibit mercury sorption (the main pathways were sketched in Fig. 5). The mercury adsorption and oxidation reactions were reversible; mercury reduction and desorption could occur after the conditions were changed. Because the adsorption process was exothermic, a fairly low temperature facilitated mercury adsorption. In contrast, the oxidation reaction
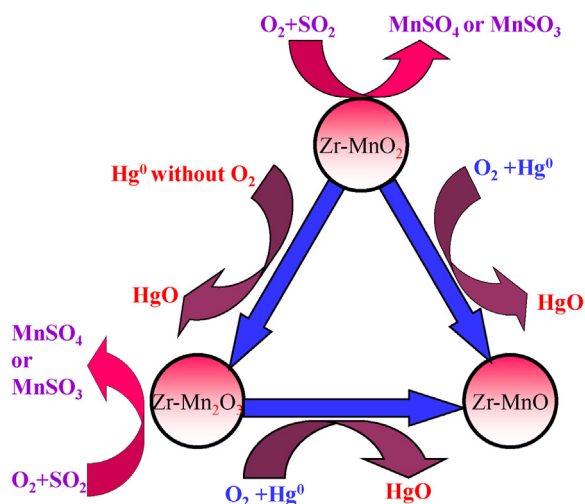
Fig. 5. Sketch of the mercury-sorbent interaction mechanism on the sorbent surface.

Fig. 7. Impact of O_2 and SO_2 on the mercury capacity of the sorbents at $100\,°C$. Space velocity: $3.8 \times 10^5\,h^{-1}$.

required energy input to overcome the reaction barrier. Therefore, temperature played an important role in the mercury removal performance of the sorbent. At low temperatures, mercury adsorbed onto the sorbent surface and was oxidized. At $350\,°C$, the oxidized mercury was decomposed and desorbed from the sorbent surface.

3.2. Mercury retention test

As shown in Fig. 6, temperature played an important role in the mercury capacity of the sorbents. In general, relatively low temperatures facilitated the adsorption of mercury on the sorbents, whereas temperatures above $200\,°C$ led to a significant decrease in the mercury capacity of the sorbents. Although zirconium oxide itself had little mercury capture capability, its doping into manganese oxide significantly improved the mercury capacity of the sorbent. This finding may be partially attributed to the enhancement of the sample reducibility, as illustrated in the TPR test. $Zr_{0.25}Mn_{0.75}O_y$, $Zr_{0.5}Mn_{0.5}O_y$, and $Zr_{0.75}Mn_{0.25}O_y$ all displayed good capacities from 75 to $200\,°C$. In particular, $Zr_{0.5}Mn_{0.5}O_y$ had a capacity of nearly 5 mg/g at $100\,°C$, which was far higher than that for the other sorbents (the comparison was shown in supporting information Table S1). This finding was also consistent with the fact that it had the highest surface area and Mn^{4+}/Mn^{3+} ratio among the sorbents studied.
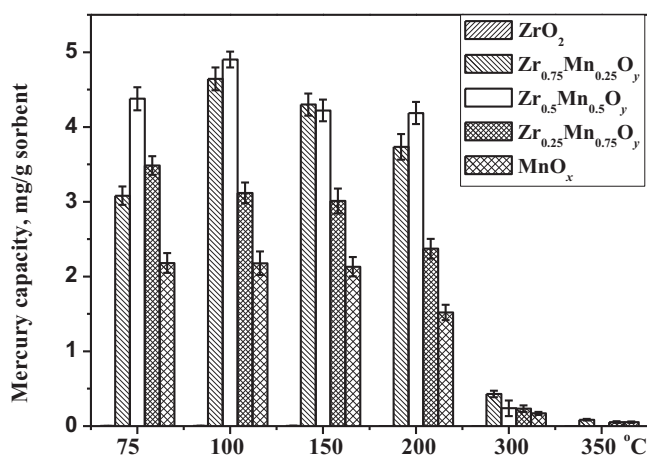
To investigate the impact of flue gas components on the mercury capacity of the sorbents, SO_2 and O_2 were added to the influent to simulate flue gas. As shown in Fig. 7, the addition of 500 ppm SO_2 into influent somewhat decreased the mercury capacity of the sorbents, possibly due to the formation of manganese sulfate, which competed for the active sites for mercury adsorption. The XPS and DPV results indicated the formation of manganese sulfate (see supporting information for DPV results). In contrast, O_2 positively affected the mercury adsorption on the sorbent. When there was no oxygen in the influent gas, the mercury capacity of the sorbents decreased significantly. This finding illustrated that oxygen may participate in the sorption process and promote the conversion of elemental mercury into its oxidized form. The mechanism is discussed later.

Due to the relatively high mercury capacity of the sorbents, the space velocities employed here were much higher than realistic values to save time. As shown in Fig. 8, when the space velocity was higher than $2.5 \times 10^5\,h^{-1}$, the mercury removal efficiency in 10 h was below 90% with N_2 and 4% O_2 as the carrying gas; however, when the space velocity was decreased to $1.9 \times 10^5\,h^{-1}$, the removal efficiency was above 95% under the same conditions. If the space velocity were decreased further, a much higher removal efficiency could be achieved. Considering that the space velocity in real cases is usually much lower, a highly desirable removal efficiency is

Fig. 6. Mercury adsorption capacities of the prepared sorbents from 75 to $350\,°C$. Space velocity: $3.8 \times 10^5\,h^{-1}$, carrier gas: $N_2 + 4\% O_2$.
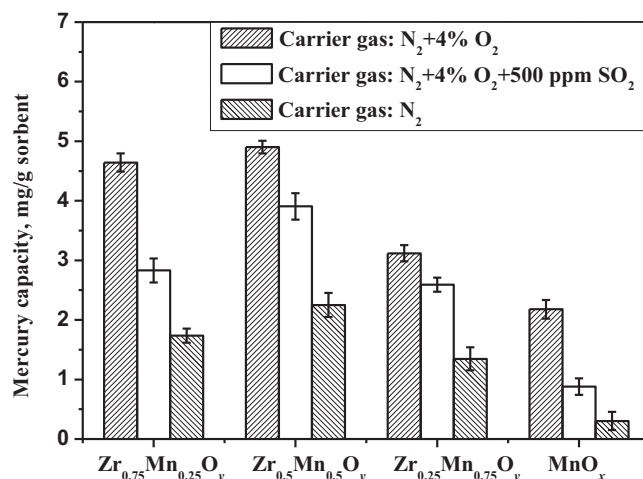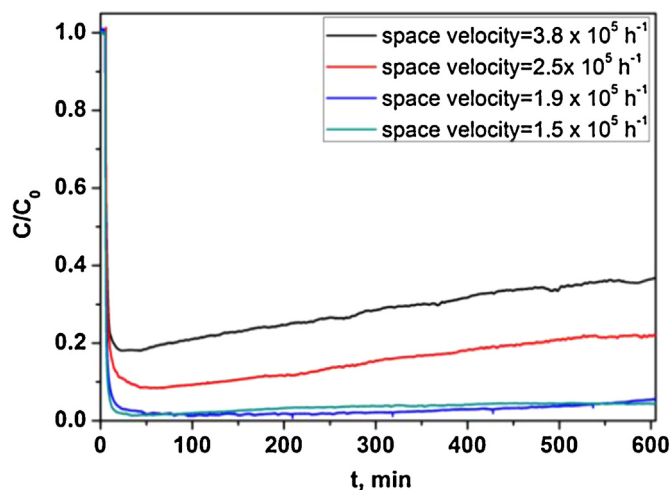

Fig. 8. Breakthrough curves under different space velocities on $Zr_{0.5}Mn_{0.5}O_y$ at $100\,°C$.
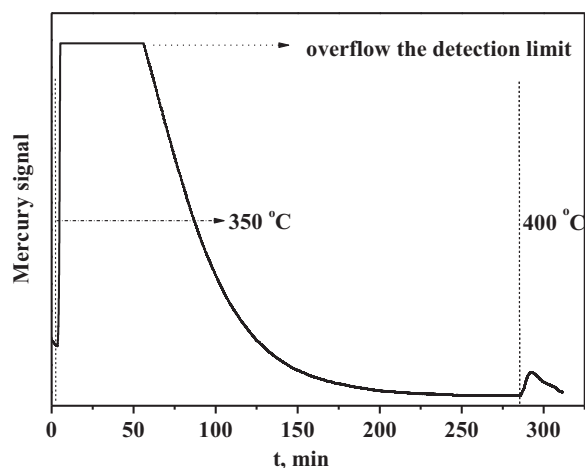
Fig. 9. Release of adsorbed mercury from spent $Zr_{0.5}Mn_{0.5}O_y$ at 350 and 400 °C.

achievable if $Zr_{0.5}Mn_{0.5}O_y$ is employed as the sorbent for mercury capture.

In addition to mercury capacity, regenerability is also very important for a new-generation sorbent. As shown in Fig. 9, the mercury adsorbed on $Zr_{0.5}Mn_{0.5}O_y$ could be facilely released through proper heating. Heating at 350 °C released most of the adsorbed mercury from the sorbent surface (XPS results revealed the release of the mercury from the sorbent surface at 350 °C) and high-concentration elemental mercury (beyond the detection limit of the detector) could be recovered by cooling. Only a very small amount of mercury was released by further elevating the temperature to 400 °C. Therefore, a much greener process could be built based on this regenerable sorbent when two parallel fix-beds are used alternately (see Fig. S2). When one sorption bed is in operation for mercury capture from flue gas, the other bed can be heated for sorbent regeneration and mercury recovery. Through this process, the mercury in flue gas can be separated and concentrated while the flue gas is decontaminated.

Furthermore, the reusability of the sorbent is also crucial for industrial application. Herein, the spent $Zr_{0.5}Mn_{0.5}O_y$ was regenerated at 350 °C after adsorbing mercury in the presence of 500 ppm SO_2 and then reused to investigate changes in its mercury removal efficiency over 10 h (see Fig. S3). For the fresh sorbent, high removal efficiency was observed. After desorbing at 350 °C and washing with water for 0, 5, and 10 min, different removal efficiencies were achieved. The sorbent lost most of its mercury capacity without washing treatment. However, its capability for mercury removal could to some extent be recovered through proper washing. The extent of the recovery depended on the washing condition. Although the total removal efficiency was decreased, a removal efficiency greater than 70% could be achieved when the desorbed sorbent was washed with water for 10 min. A much higher efficiency may be achievable if the sorbent was washed under sonication.

Combining the characterization and experimental results, it was speculated that manganese sulfate formed on the sorbent surface, covering the active sites and preventing mercury from accessing them. When the desorbed sorbent was washed with water, the soluble manganese sulfate was washed away from the surface. Therefore, the active sites on sorbent surface could be revived, and its mercury removal capability could be recovered. To test this hypothesis, the water used to wash the desorbed sorbent was collected and analyzed by an electrochemical method (DPV) with KCl solution (Fig. S4). The reducing peak potential of the DPV curve was in good agreement with that of $MnSO_4$, which indicated that the formed manganese sulfate could be facilely washed away from

the sorbent surface. Through the modification of the washing conditions, a good recovery of the mercury removal efficiency could be anticipated.

4. Conclusions

A series of novel regenerable sorbents based on Zr–Mn binary oxides has been prepared and investigated to determine their mercury capacity. $Zr_{0.5}Mn_{0.5}O_y$ outperformed the tested sorbents, with a much higher mercury capacity (5 mg/g sorbent) than the other tested sorbents and the previously reported gold- and silver-based sorbents (0.044–0.5 mg/g sorbent). High-valence manganese species facilitated the oxidation of the adsorbed elemental mercury. O_2 promoted the oxidization of the adsorbed elemental mercury by Mn^{3+} and thereby improved the mercury capacity of the sorbent. Because of competitive adsorption with elemental mercury, SO_2 would inhibit mercury adsorption and oxidation on sorbent surface. However, through proper heating and washing treatments, the spent sorbent could be facilely regenerated and used repeatedly. Meanwhile, high-concentration elemental mercury could be released and recovered by cooling. A much greener process could be anticipated based on this high-performance reusable sorbent.

Acknowledgments

Appendix A. Supplementary data

Supplementary data associated with this article can be found, in the online version, at http://dx.doi.org/10.1016/j.jhazmat. 2013.07.027.

References

[1] W.F. Fitzgerald, C.H. Lamborg, C.R. Hammerschmidt, Marine biogeochemical cycling of mercury, Chemical Reviews 107 (2007) 641–662.
[2] E.G. Pacyna, J.M. Pacyna, K. Sundseth, J. Munthe, K. Kindbom, S. Wilson, F. Steenhuisen, P. Maxson, Global emission of mercury to the atmosphere from anthropogenic sources in 2005 and projections to 2020, Atmospheric Environment 44 (2010) 2487–2499.
[3] H.Z. Tian, Y. Wang, K. Cheng, Y.P. Qu, J.M. Hao, Z.G. Xue, F.H. Chai, Control strategies of atmospheric mercury emissions from coal-fired power plants in China, Journal of the Air & Waste Management Association 62 (2012) 576–586.
[4] D.G. Streets, Q. Zhang, Y. Wu, Projections of global mercury emissions in 2050, Environmental Science and Technology 43 (2009) 2983–2988.
[5] Y.J. Zheng, A.D. Jensen, C. Windelin, F. Jensen, Review of technologies for mercury removal from flue gas from cement production processes, Progress in Energy and Combustion Science 38 (2012) 599–629.
[6] G.B. Jiang, J.B. Shi, X.B. Feng, Mercury pollution in China, Environmental Science and Technology 40 (2006) 3672–3678.
[7] A.A. Presto, E.J. Granite, Survey of catalysts for oxidation of mercury in flue gas, Environmental Science and Technology 40 (2006) 5601–5609.
[8] N. Omine, C.E. Romero, H. Kikkawa, S. Wu, S. Eswaran, Study of elemental mercury re-emission in a simulated wet scrubber, Fuel 91 (2012) 93–101.
[9] Y.F. Yang, Q.F. Huang, Q. Wang, Ignoring emissions of hg from coal ash and desulfurized gypsum will lead to ineffective mercury control in coal-fired power plants in China, Environmental Science and Technology 46 (2012) 3058–3059.
[10] H.Q. Yang, Z.H. Xu, M.H. Fan, A.E. Bland, R.R. Judkins, Adsorbents for capturing mercury in coal-fired boiler flue gas, Journal of Hazardous Materials 146 (2007) 1–11.
[11] S.J. Yang, Y.F. Guo, N.Q. Yan, D.Q. Wu, H.P. He, J.K. Xie, Z. Qu, C. Yang, J.P. Jia, A novel multi-functional magnetic Fe–Ti–V spinel catalyst for elemental

mercury capture and callback from flue gas, Chemical Communications 46 (2010) 8377–8379.

[12] J.Y. Lee, Y.H. Ju, T.C. Keener, R.S. Varma, Development of cost-effective noncarbon sorbents for Hg-0 removal from coal-fired power plants, Environmental Science and Technology 40 (2006) 2714–2720.

[13] Y. Liu, D.J.A. Kelly, H.Q. Yang, C.C.H. Lin, S.M. Kuznicki, Z.G. Xu, Novel regenerable sorbent for mercury capture from flue gases of coal-fired power plant, Environmental Science and Technology 42 (2008) 6205–6210.

[14] K. Sato, T. Kinoshita, H. Abe, Performance and durability of nanostructured $(La_{0.85}Sr_{0.15})_{(0.98)}MnO_3$/yttria-stabilized zirconia cathodes for intermediate-temperature solid oxide fuel cells, Journal of Power Sources 195 (2010) 4114–4118.

[15] J. Dong, Z.H. Xu, S.M. Kuznicki, Mercury removal from flue gases by novel regenerable magnetic nanocomposite sorbents, Environmental Science and Technology 43 (2009) 3266–3271.

[16] M. Taguchi, S. Takami, T. Adschiri, T. Nakane, K. Sato, T. Naka, Synthesis of surface-modified monoclinic ZrO_2 nanoparticles using supercritical water, CrystEngComm 14 (2012) 2132–2138.

[17] K. Sato, H. Abe, S. Ohara, Selective growth of monoclinic and tetragonal zirconia nanocrystals, Journal of the American Chemical Society 132 (2010) 2538–2539.

[18] S.J. Yang, Y.F. Guo, N.Q. Yan, D.Q. Wu, H.P. He, Z. Qu, J.P. Jia, Elemental mercury capture from flue gas by magnetic Mn–Fe spinel: effect of chemical heterogeneity, Industrial and Engineering Chemistry Research 50 (2011) 9650–9656.

[19] S.J. Yang, N.Q. Yan, Y.F. Guo, D.Q. Wu, H.P. He, Z. Qu, J.F. Li, Q. Zhou, J.P. Jia, Gaseous elemental mercury capture from flue gas using magnetic nano-sized $(Fe_{3−x}Mn_x)_{(1-delta)}O_4$, Environmental Science and Technology 45 (2011) 1540–1546.

[20] R. Xu, X. Wang, D.S. Wang, K.B. Zhou, Y.D. Li, Surface structure effects in nanocrystal MnO_2 and Ag/MnO_2 catalytic oxidation of CO, Journal of Catalysis 237 (2006) 426–430.

[21] L. Ji, P.M. Sreekanth, P.G. Smirniotis, S.W. Thiel, N.G. Pinto, Manganese oxide/titania materials for removal of NOx and elemental mercury from flue gas, Energy & Fuels 22 (2008) 2299–2306.

[22] S.J. Yang, Y.F. Guo, N.Q. Yan, D.Q. Wu, H.P. He, Z. Qu, C. Yang, Q. Zhou, J.P. Jia, Nanosized cation-deficient Fe–Ti spinel: a novel magnetic sorbent for elemental mercury capture from flue gas, ACS Applied Materials & Interfaces 3 (2011) 209–217.